JBIC Journal of Biological Inorganic Chemistry
https://doi.org/10.1007/s00775-024-02087-5

ORIGINAL PAPER

# Insights into periplasmic nitrate reductase function under single turnover

**Jennifer McGarry[1] · Breeanna Mintmier[2] · Mikayla C. Metzger[2] · Nitai C. Giri[2] · Nicholas Britt[1] · Partha Basu[2] · Jarett Wilcoxen[1]**

Received: 19 September 2024 / Accepted: 13 November 2024
© The Author(s), under exclusive licence to Society for Biological Inorganic Chemistry (SBIC) 2024

## Abstract

Nitrate reductases play pivotal roles in nitrogen metabolism by leveraging the molybdopterin cofactor to facilitate the reduction of nitrate to nitrite. Periplasmic nitrate reductases (NapA) utilize nitrate as a terminal electron acceptor when oxygen is limiting, helping to drive anaerobic metabolism in bacteria. Despite extensive research into NapA homologs, open questions about the mechanism remain especially at the molecular level. More broadly, little is understood of how the molybdopterin cofactor is tuned for catalysis in these enzymes enabling broad substrate scope and reactivity observed in molybdenum-containing enzymes. Here, we have prepared NapA from *Campylobacter jejuni* under single turnover conditions to generate a singly reduced enzyme that can be further examined by electron paramagnetic resonance (EPR) spectroscopy. Our results provide new context into the known spectra and related structures of NapA and related enzymes. These insights open new avenues for understanding nitrate reductase mechanisms, molybdenum coordination dynamics, and the role of pyranopterin ligands in catalysis.

**Keywords** Nitrate reductase · Molybdenum · Molybdopterin · Electron paramagnetic resonance · *Campylobacter jejuni*

## Abbreviations

| | |
|---|---|
| *NapA* | Periplasmic nitrate reductase |
| *CjNapA* | *Campylobacter jejuni* Periplasmic nitrate reductase |
| *DdNapA* | *Desulfovibrio desulfuricans* Periplasmic nitrate reductase |
| *EPR* | Electron paramagnetic resonance |
| $MV^{ec}$ | Electrochemically reduced methyl viologen |
| *WT* | Wild type |
| *HEPES* | 2-[4-(2-Hydroxyethyl)piperazin-1-yl]ethanesulfonic acid |
| *CW* | Continuous wave |
| *DMSO* | Dimethyl sulfoxide |

✉ Partha Basu
Basup@iu.edu

✉ Jarett Wilcoxen
Jarettw@uwm.edu

[1] Department of Chemistry and Biochemistry, University of Wisconsin- Milwaukee, Milwaukee, WI 53211, USA

[2] Department of Chemistry and Chemical Biology, Indiana University Indianapolis, Indianapolis, IN 46202, USA

## Introduction

Nitrate reductases are molybdenum (Mo)-containing enzymes found in the assimilatory or dissimilatory pathways of nitrogen metabolism [1–3]. *Campylobacter jejuni*, an emerging antibiotic-resistant pathogen that is a major cause of food borne illness [4], has a single nitrate reductase localized to the periplasm (periplasmic nitrate reductase, NapA) that presents an intriguing therapeutic target necessitating an in-depth molecular level understanding of the enzyme and mechanism. Nitrate reductases are well-described in the literature, especially periplasmic nitrate reductase from organisms such as *Desulfovibrio desulfuricans, Cereibacter sphaeroides*, *Cupriavidus necator*, *Paracoccus pantotrophus,* and *Escherichia coli*, which has been studied through crystallography, kinetics, and spectroscopy [1, 2, 5–7]. However, there are significant gaps in our understanding of cofactor function and there are controversial literature reports regarding the mechanism of action. A particularly intriguing aspect is the identification of an all-sulfur coordination sphere in crystal structures from *D. desulfuricans* NapA [8]. Four sulfur atoms come from two pyranopterin guanosine dinucleotide ligands that coordinate bidentate through an ene-dithiolate, one comes from a cysteine from

Published online: 04 December 2024

the peptide, and one is a terminal thiol/sulfido [8]. We have recently investigated the coordination environment of *C. jejuni* (*Cj*NapA) by X-ray absorption spectroscopy and found there is in fact a terminal oxo and not a terminal thiol/sulfido as shown in the structural report on *D. desulfuricans* NapA [9]. In light of this, a mechanism was proposed, as shown in Fig. 1a, where nitrate coordinates to the enzyme when reduced (step 1), followed by oxygen atom transfer and dissociation of the product nitrite (step 2). There is then internal electron transfer and reduction of the molybdopterin via the $[Fe_4S_4]$ and an external electron donor (methyl viologen in vitro or the heme-containing NapB in vivo) to complete the catalytic cycle [9–12].

We have taken advantage of this catalytic cycle under single turnover conditions where the enzyme, after reducing nitrate is left with a single reducing equivalent to yield a partially reduced molybdopterin that is amenable to further study by electron paramagnetic resonance (EPR) spectroscopy. EPR is highly sensitive to subtle changes in the primary and secondary coordination sphere and, importantly for Mo enzymes, reports the electronic structure of the metal center during catalysis. Mechanistic insights gained using EPR in the study of Mo enzymes have had a profound impact, often identifying inhibited states and geometries of active enzymes not revealed by other means, such as protein crystallography [13–16]. Here, we have identified an EPR-active intermediate in the catalytic cycle, as shown in Fig. 1a, structure iv, and propose a model for this species. The model is developed considering the spectroscopic data of relevant members of the DMSO reductase family, computational models of NapA, and our own recent work with *Cj*NapA [5, 9]. Our data suggest the conservation of the active site geometry during the catalytic cycle and an important role in the secondary binding interactions near the cofactor in modulating its electronic structure of the cofactor.

## Methods

### Materials

All reagents and materials were purchased from ThermoFisher or Millipore-Sigma at ACS reagent grade or better unless otherwise indicated. All solutions were prepared

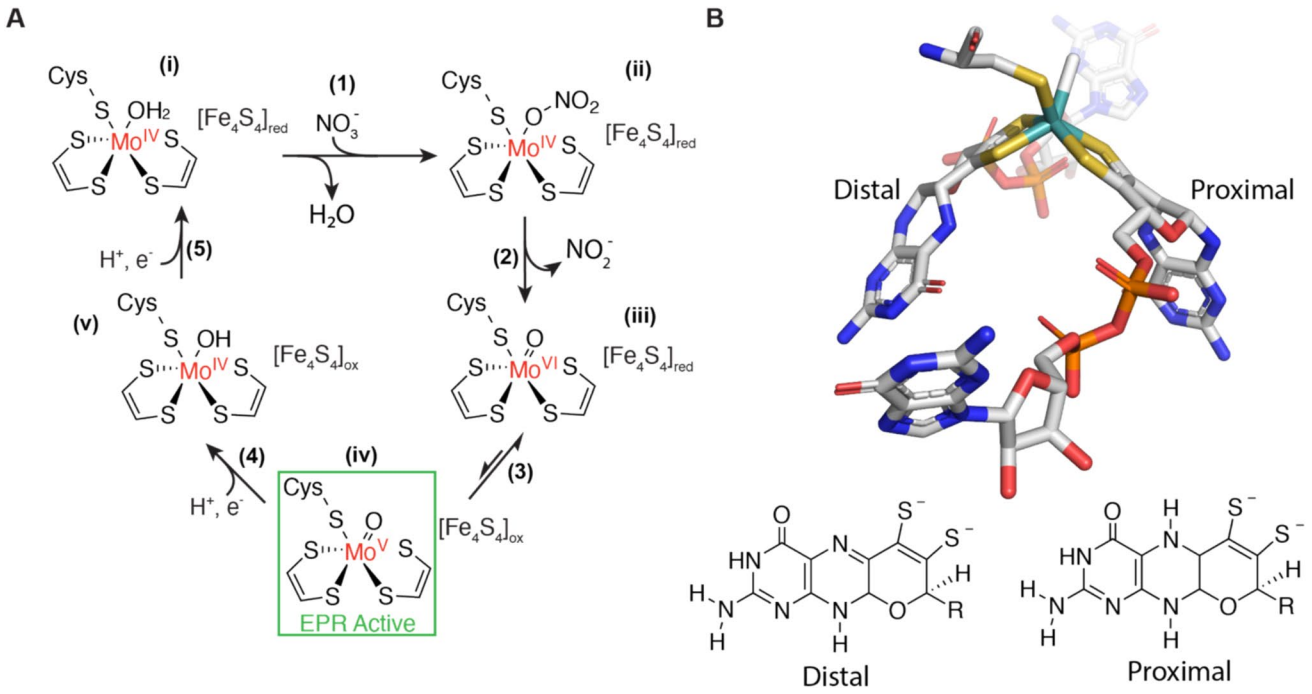


**Fig. 1** Mechanism and active site structure of periplasmic nitrate reductases. **A** The reaction mechanism proposed for NapA resembles many oxygen atom transfer reactions catalyzed by molybdenum enzymes [3]. As with many molybdenum- and tungsten-containing enzymes, the metal cycles through single electron reduction/oxidation and formal two-electron oxidation/reduction events during catalysis. The reducing equivalents in NapA are supplied to Mo sequentially by a nearby iron-sulfur cluster near the proximal pyranopterin. The EPR-active species, highlighted in green, is generated via substrate reduction and internal electron transfer. **B** The cofactor resembles that found in NapA from *Desulfovibrio desulfuricans* (PDB ID: 2jip), where Mo is coordinated by two inequivalent pyranopterins, present as the pyranopterin guanosine dinucleotide (the dinucleotide moiety is shown as R), a cysteine. Lewis structures of the distal and proximal pyranopterins are provided for clarity.

using deionized water filtered with a MilliQ water purification system (18 MΩ cm resistivity).

## Cell growth, protein expression, and purification

WT *Campylobacter jejuni* (strain RM1221) NapA *(Cj*NapA*)* expression and purification were done as previously described. [11] Briefly, *Escherichia coli* K12 (New England Biolabs Shuffle T7 lysY #C3027) cells were transformed with the pBM10C plasmid using heat shock. Transformed *E. coli* cells successfully formed colonies on LB medium supplemented with 30 µg/mL kanamycin. Inoculated cultures were grown overnight at 37 °C, then transferred to 10 L of fresh autoinduction medium containing 12 g/L peptone, 24 g/L yeast extract, 1 g/L glucose, 2 g/L lactose, 0.50% (v/v) glycerol, and 90 mM potassium phosphate buffer, pH 7.00. The cultures were supplemented with kanamycin (30 µg/mL) and $Na_2MoO_4$ (1 mM). NapA expression was induced by the lactose present in the medium. Expression was conducted at 25 °C for 48 h while shaking at 250 rpm. Cells were collected by centrifugation at 3750 × g at 4 °C. The cell pellet was resuspended in an ice-cold buffer containing 50 mM HEPES, 300 mM NaCl, and 10 mM imidazole at pH 7.00.

Cells were lysed by ultrasonication using 30s pulses in 45s intervals over 10 min in an ice bath. The lysate was centrifuged at 11,600 × g for 1h at 4 °C. The soluble fraction was loaded on a HisTrap HP 5 mL prepacked column (Cytiva Life Sciences), and separation was conducted with an ÄKTA Pure FPLC (Cytiva Life Sciences). NapA was eluted with 250 mM imidazole. The fractions were pooled and concentrated using 30 kDa cutoff centrifugal filters (Millipore). The concentrated protein was loaded onto a HiPrep 16/60 Sephacryl S-200 size exclusion column (Cytiva Life Sciences). The resulting NapA fractions were pooled, concentrated, and stored in buffer containing 50 mM HEPES pH 7.00 at −80 °C.

## *Electron* paramagnetic resonance spectroscopy

Samples for X-band (~ 9.4 GHz) EPR spectroscopy were prepared under single turnover conditions by titrating to full reduction approximately 250 µL of 100–200 µM NapA in 50 mM HEPES pH 7.0, 200 mM NaCl, with dithionite or electrochemically reduced methyl viologen ($MV^{ec}$) under anoxic conditions (< 0.5 ppm $O_2$) in a LC-100 (LC Technology Solutions Inc) glove box. Methyl viologen was electrochemically reduced by bulk electrolysis using a Model 600E potentiostat (CH Instruments). We applied a −500 mV potential to 1 mM methyl viologen (methyl viologen midpoint potential −446 mV vs NHE at 30 °C) [17] in 50 mM HEPES pH 7.0, 200 mM NaCl with a platinum mesh working electrode, platinum counter electrode, and Ag/AgCl reference electrode monitoring the current. The reduction of methyl viologen was verified by UV–vis spectroscopy monitoring the increase at 600nm for the monocation reduced state of methyl viologen. The reduction of NapA was monitored by bleaching of the 420 nm absorbance consentient with reduction of the $[Fe_4S_4]$ cluster. We also monitored 600 nm to ensure there was no detectable reduced methyl viologen that may result in steady-state conditions as opposed to the single turnover conditions. The protein was then added to a 4 mm OD quartz sample tube (Wilmad) containing 10 µL of 10 mM nitrate in the same buffer. Samples were immediately frozen in the glovebox in an ethanol/dry ice bath, capped with a rubber stopper, removed from the glovebox, and immediately placed in liquid nitrogen. Buffer-exchanged samples were reduced and reacted with nitrate as above, followed by the removal of nitrate and reductants by PD10 gel filtration column in the glovebox. The protein was then concentrated, placed in an EPR tube, and frozen as above. Frozen samples were stored in liquid nitrogen until use. Continuous wave (CW) spectra were collected using a Magnettech MS5000 spectrometer (Freiberg Instruments) equipped with a liquid nitrogen cryostat with a temperature and gas-flow controller. NapA samples were measured under non-saturating conditions at 150 K using 9.4 GHz microwave frequency, 2 mW microwave power, 120 s sweep time 3G modulation amplitude. The EPR signal of NapA was quantified using a 100 µM and 200 µM Cu-EDTA spin standard. The spectra were corrected for temperature, power, modulation amplitude, and quality factor before double integration to yield a spin concentration for each sample [18]. Spectra analysis, plotting, and simulations were performed using Easyspin (Easyspin.org) in Matlab R2019a (Mathworks Inc). Spectra are shifted from their collection frequencies, which vary from 9.465 to 9.485 GHz, to a common 9.475 GHz for plotting and spectral comparison using the following equation:

$$x(data@9.475GHz) = x(data@origfreq.) * \frac{9.475}{\nu(ofcollecteddatainGHz)}$$

### NapA activity assay

Nitrate reductase activity was measured spectrophotometrically by monitoring the oxidation of reduced methyl viologen ($MV^{ec}$) at 600 nm as previously described or by monitoring the oxidation of dithionite at 310 nm in an assay that parallels the assay with methyl viologen, SI Fig. 1. [11, 19, 20] We note that the heterologous expression system and purification of *Cj*NapA used here result in enzyme activity is consistent with that of other characterized NapA homologs that have been purified under native expression conditions and has been demonstrated to have a tenfold higher catalytic efficiency ($k_{cat}/K_m$) than other NapA homologs. [2, 5, 11]

## Results and discussion

Samples of approximately 200 µM of WT *Cj*NapA were frozen after being titrated to full reduction with 10 mM of electrochemically reduced methyl viologen ($MV^{ec}$) or 10 mM of dithionite, and then oxidized with nitrate. Importantly for this work, the enzyme was frozen under single turnover conditions to yield a state that is reflective of the active enzyme. Reducing *Cj*NapA with $MV^{ec}$ then re-oxidizing it with the substrate and rapidly freezing the sample produces a distinct EPR spectrum, as shown in Fig. 2A, that we have termed Species 1 (structure iv in Fig. 1). This species is similar to the 'Turnover' species described for the *Dd*NapA. We note a slight shift in the *g*-values, [1.999, 1.990, 1.982] vs [1.996, 1.989, 1.978] for *Dd*NapA and *Cj*NapA, respectively. [21] Given that the enzyme is from two different species with slight dissimilarities in the binding pocket of the cofactor, this is in excellent agreement. When dithionite is used as a reductant, we note the enzyme stays reduced and is not active in steady state or oxidative half reaction assays. When the enzyme reduced by dithionite and is exposed to air, an EPR spectrum (SI Fig. 3) is observed consentient with previously reported (additional details provided in the Supplementary Information). [21–24]

The signal-giving species in all the samples prepared account for approximately 10–20% of the total protein concentration in the sample as determined by Bradford assay in agreement with previous work with NapA homologs. [21, 22, 24, 25] The spin concentration varied within this range

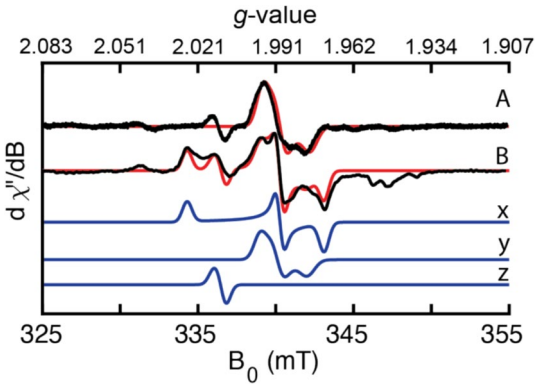


**Fig. 2** EPR Spectra of NapA. EPR spectra (Black) and simulations (Red) of the wildtype *Cj*NapA reduced with methyl viologen (MV) and partially oxidized with nitrate. When immediately frozen after addition of nitrate we observe a single species **A**, termed 'Species 1', When **A** is buffer exchanged, a complex spectrum comprised of three species is observed **B**. The two major components are a newly identified 'Species 2' (x) and some remaining 'Species 1' (y). The simulation also includes an organic radical (z) that corresponds to 1–2% of the sample. EPR spectra were recorded at 150K, 9.4 GHz, 2 mW power, 3 G modulation amplitude.

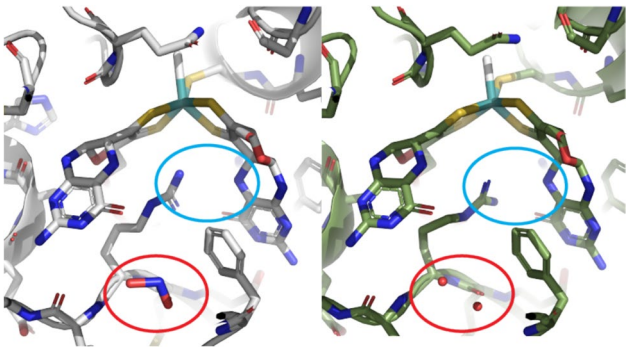

**Fig. 3** Structure Models of NapA with and without nitrite near the molybdenum cofactor but distant from the site of catalysis. Nitrite modeled in the crystal structure (PDB: 2jiq, left), circled in red, is below the plane of the pyranopterins in a location occupied by two water molecules in other structure models (PDB:2jip, right). We note additional movements of Arg617 in the structure that hydrogen bonds to N-5 of one pyranopterin (blue circle)

depending on the purified protein batch used and specific sample preparation. According to Fig. 1a model, the single turnover conditions mean that the Mo center is 2-electron reduced and the [$Fe_4S_4$] center remained 1-electron reduced in the fully reduced enzyme prior to nitrate addition (Fig. 1a, structure i). Upon addition of nitrate, the Mo center is oxidized to the $Mo^{VI}$ state via an oxygen atom transfer, which initially generates the EPR-silent species Fig. 1, structure iii. We conjecture that the concentration of the EPR-active $Mo^{V}$ species (Fig. 1, structure iv) is determined by Fig. 1 step 3 equilibrium.

The EPR spectra are described by *g*-values, but the relationship of those *g*-values to structure can be simplified using the span and skew of the *g*-values [26]. The span (span = $g_1 - g_3$) describes the anisotropy and overall width of the spectra (for example, 0.018 for 'Species 1'). The span is heavily influenced by the magnitude of the spin–orbit coupling of the individual atoms that make up the ground state and the orbital mixing between the ground state and nearby excited states. Large spin–orbit couplings and small energy gaps between the ground state and excited states result in a large shift in the *g*-values from the value of a free electron ($g_{free} = 2.0023$). The skew (skew = $\frac{g_1 - g_2}{g_1 - g_3}$) captures the rhombicity of the *g*-values with values near 0 or 1 representing an axial spectrum and values near 0.5 representing a fully rhombic spectrum. The skew is sensitive to the symmetry of the metal site and energetic splitting of the d-orbitals. To illustrate the relationship between idealized geometry and predicted EPR symmetry, we use an example of the common geometry found in DMSO reductase family enzymes and the only geometry of the active site identified by X-ray crystallography studies, Fig. 1B, the six-coordinate trigonal prismatic geometry. The idealized $D_{3h}$ (trigonal prismatic)

yields a 4 $d_{z^2}$ [1] in the ground state where shifts arise from the energetic spacing between the $d_{z^2}$ and the energetically degenerate$d_{yz}$, $d_{xz}$ orbital pair, also yielding an axial line shape with one $g$-value ($g_z$) near 2. Distortions away from idealized symmetry via asymmetric changes in bond angle or length result in shifts in the excited states, lifting the degeneracy and resulting in more rhombic spectra.

Applying the above criteria to our spectra, 'Species 1' (Fig. 2A), previously described as belonging to the 'High $g$' EPR species family characterized by a spectra with $g$-values near $g = 1.99$ with little span, has a span of 0.018 and a skew of 0.39 [7, 27]. This span and skew depart from the idealized $D_{3h}$ geometry and suggest little mixing between the ground state and excited states. Notably, 'Species 1' is similar to that observed in a related enzyme, DMSO reductase. DMSO reductase contains a similar coordination sphere (two pyranopterins, an oxo, and a peptide ligand in a near trigonal prismatic geometry) but has a serine instead of the cysteine peptide ligand. Replacing serine with cysteine in DMSO reductase to make the ligand environment similar to that of NapA shifts the EPR $g$-values to values like those observed for 'Species 1' [16]. DMSO reductase is one of the best characterized bis-pyranopterin enzymes, with extensive kinetics, X-ray spectroscopy, X-ray crystallography, and EPR spectroscopy having been used to validate models of intermediates in the mechanism [16, 28–36]. Importantly, this includes models of the $Mo^V$ coordination environment where the overall geometry is roughly trigonal prismatic, similar to the EPR-active state in Fig. 1, with slight distortion and asymmetry induced by the one oxygen ligand lifting the degeneracy of the $d_{yz}$ and $d_{xz}$ orbitals. This yields a rhombic line shape that is compressed due to well-separated excited states with one $g$-value ~ 2 and the other two with slight shifts to a higher field (lower $g$-value). [16]

Computational approaches can often provide insight into the underlying geometry of EPR species, especially in small-molecule models. Recent computational studies of the NapA EPR spectra led the authors to conclude that spectra similar to 'Species 1' can be modeled as a six-sulfur-coordinate species. The study found that a partially geometry-optimized six-sulfur-coordinate model complex, based on an earlier X-ray crystallography model [8], yielded an EPR spectrum that approximated the experimental spectra (Table 1, DFT-NapA$^{\$}$, partial disulfide) [27]. In the same study, geometry-optimized models where the Mo is coordinated by a bis-enedithiolate, hydroxide, and thiol ligands yielded $g$-values that are similar but uniformly shifted to higher $g$-value by ~ 0.009 from 'Species 1' (Table 1, DFT-NapA$^{\#}$, hydroxo). Perfect agreement between computationally derived EPR $g$-values and those measured from the enzyme active sites is rare. Many features that can modulate the $g$-values, such as the full cofactor and surrounding peptide environment, are missing from these models and would be needed to more accurately reproduce the enzyme state. Studies that examined the computed models of Mo enzymes found that the extent of pyranopterin inclusion in the model had a clear influence on the spectrum generated, suggesting that inaccuracies are introduced with truncated cofactors [37]. This is in addition to the influence of bond lengths and ligand angles, and torsion/folding between the pyranopterin equivalents, and starting geometry [38, 39]. One can strive to use the geometries derived in the crystal structure, but these are static representations of typically fully reduced or fully oxidized enzyme that has a dynamic primary coordination sphere, complex electrostatic and hydrogen bonding environment. We propose a model for 'Species 1' when excess nitrate and/or nitrite is present (Fig. 1, structure iv) where the Mo is coordinated by two pyranopterin equivalents, a sulfur donor, and a hydroxy ligand. This model is consistent with the Cys variant of DMSO reductase ($g$-values in Table 1) and recent Extended X-ray Absorption Fine Structure data of the nitrate oxidized resting state of *Cj*NapA [9]. The model represents an intermediate that can be generated under the single turnover conditions used in this study, and that is common in most mechanisms proposed for NapA. [16]

If instead of immediately freezing it, the $MV^{ec}$-reduced and substrate-oxidized sample is buffer exchanged to remove any excess substrate or products formed under anoxic conditions and then frozen, a very different spectrum is obtained (Fig. 2B). The buffer-exchanged sample is complex but reproducible (> 5 times), and can be modeled with a combination of three identified species, comprising approximately 85% (± 3%) from a species with a large span with $g$-values of [2.024, 1.9885, 1.972] (denoted 'Species 2' in Table 1, Fig. 2x), approximately 15% (± 3%) from 'Species 1' (Fig. 2y) that is present before buffer exchange (Fig. 2A), and 1–2% (± 0.5%) of an organic radical, (Fig. 2z). The organic radical has been observed previously [40]. To account for its intensity in the simulations, a $g$-tensor ([2.0145, 2.0125, 2.0105]) and an isotropic broadening of 15 MHz was determined from spectra of Species 1, in which the radical also appears, but with less signal overlap (SI Fig. 2). Although present in the spectra, we have not simulated the contributions to the line shape from the $^{95}$Mo (~ 16% abundance) and $^{97}$Mo (~ 10% abundance) given the complexity involved; such a simulation requires 12 values to be fit by means of a hyperfine tensor, hyperfine strain tensor, nuclear quadrupole, and Euler angles. Currently, there is little other data to support such a simulation and few examples in the literature to provide guidance. Higher resolution pulse EPR experiments planned will provide a better foundation for simulations of the $^{95}$Mo and $^{97}$Mo contributions.

The overall line shape of the 'Species 2' (Fig. 2 × contribution to Fig. 2B) represents a significant deviation from the published EPR spectra for WT NapA [1, 2]. There is a slight

**Table 1** EPR simulation parameters of DMSO reductase family enzymes *

| Species | Enzyme | Signal name | $g_1$ | $g_2$ | $g_3$ | $g_{Avg}$ | Span | Skew | Ref |
|---|---|---|---|---|---|---|---|---|---|
| *Campylobacter jejuni* | NapA | Dithionite reduced | 1.999 (15)* | 1.9892 (15)* | 1.983 (15)* | 1.9904 | 0.016 | 0.63 | This work |
| *Campylobacter jejuni* | NapA | Species 1 | 1.996 (25)* | 1.9893 (25)* | 1.978 (30)* | 1.9878 | 0.018 | 0.39 | This work |
| *Campylobacter jejuni* | NapA | Species 2 | 2.024 (20)* | 1.9885 (15)* | 1.972 (20)* | 1.9948 | 0.052 | 0.67 | This work |
| *Campylobacter jejuni* | NapA | C176A | 2.0172 | 1.9879 | 1.9647 | 1.9899 | | | [9] |
| *Paracoccus denitrificans* | NapA | High g [resting] | 1.9985 | 1.9902 | 1.9806 | 1.9898 | 0.018 | 0.46 | [23] |
| *Paracoccus denitrificans* | NapA | High g [nitrate] | 1.9988 | 1.9886 | 1.9815 | 1.9896 | 0.017 | 0.59 | [23] |
| *Paracoccus denitrificans* | NapA | High g [nitrate] | 1.9980 | 1.9890 | 1.9810 | 1.9893 | 0.017 | 0.53 | [23] |
| *Desulfovibrio desulfuricans* | NapA | Nitrate | 2.0000 | 1.9900 | 1.9810 | 1.9903 | 0.019 | 0.53 | [21] |
| *Desulfovibrio desulfuricans* | NapA | Turnover $^{14}N/^{15}N$ | 1.9990 | 1.9900 | 1.9820 | 1.9903 | 0.017 | 0.53 | [21] |
| *Desulfovibrio desulfuricans* | NapA | Low potential | 2.016 | 1.987 | 1.964 | 1.989 | 0.052 | 0.67 | [21] |
| *Synechococcus sp. PCC 7942* | NarB | Dithionite reduced | 1.9970 | 1.9900 | 1.9820 | 1.9897 | 0.015 | 0.47 | [40] |
| *Synechococcus sp. PCC 7942* | NarB | C148A | 2.0250 | 1.9900 | 1.9700 | 1.9950 | 0.055 | 0.64 | [40] |
| *Rhodobacter sphaeroides* | DMSOR | DMSOR WT* | 1.9924 | 1.9815 | 1.9650 | 1.9796 | 0.027 | 0.4 | [16] |
| *Rhodobacter sphaeroides* | DMSOR | DMOSR S147C* | 1.9981 | 1.9903 | 1.9851 | 1.9912 | 0.013 | 0.6 | [16] |
| *Rhodobacter sphaeroides* | DMSOR | | 1.9922 | 1.9818 | 1.9673 | 1.9804 | 0.025 | 0.42 | [47] |
| *Rhodobacter sphaeroides* | DMSOR | | 1.9906 | 1.9833 | 1.9611 | 1.9783 | 0.029 | 0.25 | [47] |
| *Rhodobacter capsulatus* | DMSOR | | 1.9988 | 1.9885 | 1.9722 | 1.9865 | 0.027 | 0.39 | [47] |
| *Cupriavidus necator* | FdsDABG | | 2.0100 | 2.0020 | 1.9920 | 2.0013 | 0.018 | 0.44 | [48] |
| *Desulfovibrio desulfuricans* | FDH | WT-Formate | 2.0120 | 1.9960 | 1.9850 | 1.9977 | 0.027 | 0.59 | [49] |
| *Escherichia coli* | FDH | | 2.0940 | 2.0010 | 1.9900 | 2.0283 | 0.104 | 0.89 | [49] |
| DFT-NapA[#] | Oxo | | 2.023 | 1.983 | 1.9670 | 1.9910 | 0.056 | 0.71 | [27] |
| DFT-NapA[#] | Hydroxo | | 1.987 | 1.982 | 1.969 | 1.9793 | 0.018 | 0.28 | [27] |
| DFT-NapA[#] | Nitrate Bound | | 2.000 | 1.980 | 1.968 | 1.9827 | 0.032 | 0.63 | [27] |
| DFT-NapA[#] | Six Sulfur | | 2.019 | 1.992 | 1.981 | 1.9973 | 0.038 | 0.71 | [27] |
| DFT-NapA[#] | Six Sulfur- Partial Disulfide | | 2.018 | 2.011 | 1.975 | 2.0013 | 0.043 | 0.16 | [27] |
| DFT-NapA[$] | Six Sulfur- Partial Disulfide | | 2.006 | 1.996 | 1.981 | 1.9933 | 0.028 | 0.36 | [27] |

[*]—anisotropic linewidth, in MHz, used in simulations

[#]- geometry optimized

[$]—partial geometry optimization

*DFT-NapA* Density functional theory model of napa, *DMSOR* Dimethyl sulfoxide reductase, *NapA* periplasmic

shift in the skew, suggesting a slightly more distorted geometry or ligand environment, and a significant increase in the span suggesting much lower lying excited states. Overall, the EPR spectrum for 'Species 2' is similar to the C176A variant of CjNapA, which has the Cys ligand replaced with a hydroxide albeit with *g*-values shifted to lower magnetic fields (higher *g*-values) [9]. The coordination environment of the C176A variant is described as having a bis-pyranopterin, oxo, and hydroxy/water ligands. A shift in *g*-value(s) to lower field is often observed in Mo enzymes when the ligand is changed from oxygen to sulfur or sulfur to selenium due to the increased covalency and spin–orbit coupling of the ligand and accounts for the differences in the spectra [41, 42]. The covalency effect on the EPR spectrum is well

described in the sulfite oxidase family enzymes, especially methionine sulfoxide reductase that has been extensively characterized by spectroscopic and computational methods to find a direct impact on the identity of the ligand and corresponding shift in the EPR features [14, 43]. In addition, an EPR spectrum from *D. desulfuricans* similar to 'Species 2' was observed when reduced by spectropotentiometric titrations, identified as the 'Low potential' species, but its relevance to the catalytic cycle or rationale for its deviation from the spectrum under turnover with nitrate (similar to what we observe for 'Species 1') is not clear in previous work [21]. Taking a closer look at the *g*-values that describe the 'Low potential' species, the *g*-values are nearly identical to what we observe for C176A, suggesting this species identified in *D. Desulfuricans* corresponds to a species where the ligating Cys has been displaced by water or hydroxide. Taking into consideration the active site geometry in available crystal structures of DMSO reductase family members, and especially homologs of NapA, we model 'Species 2' as a roughly trigonal prismatic geometry with five sulfur ligands (four from the pyranopterins, one from the peptide) and an oxygen ligand, likely an oxo given the lack of observable proton hyperfine coupling in the EPR spectrum and increased asymmetry in the ligand environment. This is supported by computational work where Mo coordinated by a bis-enedithiolate, a terminal oxo, and thiol ligand has computed *g*-values of [2.023 1.983 1.967], in excellent agreement with our experimental results for 'Species 2' with *g*-values of [2.024 1.9885 1.972]. [27]

We rationalize the shift from the 'Species 1' to 'Species 2' spectrum as a change in the interaction between the pyranopterins and Mo that results in a narrowing of the gap between the ground state and excited states induced by increased charge transfer character of the bis-dithiolene ligation [8, 44]. Two crystal structures of *Dd* NapA have been reported (2jip and 2jiq), where one (2jiq) was soaked with $NO_3^-$. From these structures, the authors identified possible binding sites of the substrate nitrate and product nitrite [8]. Given the high sequence similarity and predicted fold of NapA used in this study, we have high confidence in using these structures as a model for the *C. jejuni* NapA [2]. The structure 2jiq, given in Fig. 3, displays a subtle shift in the pyranopterins relative to the 2jip structure, and notably, a nitrite below the plane of the pyranopterins that replaces two water molecules seen in the 2jip structure. In addition, $Arg^{617}$ shifts from being hydrogen bonded to two of the dithiolene sulfurs, ~ 3.2 Å away in the $NO_3^-$ soaked 2jiq structure, to more electrostatic interaction, ~ 4 Å away in the $NO_3^-$ free 2jip structure. The binding of $NO_3^-$ or $NO_2^-$ changes both the electrostatic environment near the π plane of the cofactor and the hydrogen bonding interactions of the nearby peptide residues. Such a change near the pyranopterins likely influences the electronic structure of the cofactor, leading to a larger gap in the ground state and excited states in the single turnover sample where $NO_3^-$ or $NO_2^-$ are present. Removal of the $NO_3^-$ or $NO_2^-$ by buffer exchange then results in Species 2.

## Conclusion

We have identified a new EPR species of NapA, shown in Fig. 2B, and propose a simple structural model to explain it that is consistent with the currently accepted kinetic models and requires minimal changes to the geometry and ligand environment of existing EPR species, whose structures have been under recent debate. [8, 11, 27, 45, 46] We have framed our model in the context of other members of the DMSO reductase family with similar ligand environments and geometry. Based on precedent from other DMSO reductase family enzymes, we propose that the active site under single turnover has trigonal prismatic geometry. The species generated after the removal of reactants and products results in substantial changes to the line shape that can be rationalized by changes to the electrostatic environment of the cofactor without needing to invoke large changes in the overall geometry, which is constrained in the peptide environment. In this way, the new structure is consistent with the available structures of NapA and other members of the DMSO reductase family.

When this work is put in context with the active site variants, in which the ligating Cys has been varied to Asp or Ser while still maintaining some activity, and the X-ray absorption spectroscopy studies of *Cj*NapA, the resulting model suggests that the enzyme does not contain six sulfurs when undergoing turnover with nitrate [5, 9]. We highlight the potential importance and impact of the electrostatic and hydrogen bonding environment near the pyranopterin ligands and the observed changes in the electronic structure and resulting spectra. As noted in previous computational work, these enzymes are complex systems that are highly sensitive to the environment of the cofactor and would benefit from detailed electronic structural studies of the molybdenum and tungsten cofactors and from detailed QM/MM calculations to examine the dynamics of the binding pocket and modulations of the electronic structure of the cofactor. [27, 37–39]

**Supplementary Information** The online version contains supplementary material available at https://doi.org/10.1007/s00775-024-02087-5.

**Acknowledgements** We gratefully acknowledge financial support for this work from the UWM Office of Research (to JW), the National Science Foundation (CHE 2003752 to PB) and the National Institutes of Health (GM 139064 to PB) for partial financial support of this work.

**Authors' contributions** J.M., N.B., B.M., and M.C.M. purified the protein used in these studies. J.M., N.B., and J.W. prepared samples,

carried out experiments, and data analysis. J.M., M.C.M, N.C.G, P.B, and J.W. wrote the main manuscript. J.W. Prepared figures. All authors reviewed the manuscript.

**Funding** This study was supported by National Science Foundation, CHE 2003752, National Institute of General Medical Sciences, GM 139064.

**Data availability** Data from this study are available from the corresponding author upon request.

## Declarations

**Conflict of interest** The authors declare no competing interests.

**Ethical approval** Not applicable.

## References

1. Magalon A, Ceccaldi P, Schoepp-Cothenet B (2017) The prokaryotic Mo/W-bisPGD enzymes family. Molybdenum Tungsten Enzym: Biochem 5:143–191
2. Sparacino-Watkins C, Stolz JF, Basu P (2014) Nitrate and periplasmic nitrate reductases. Chem Soc Rev 43(2):676–706
3. Hille R, Hall J, Basu P (2014) The mononuclear molybdenum enzymes. Chem Rev 114(7):3963–4038
4. Altekruse SF, Stern NJ, Fields PI, Swerdlow DL (1999) Campylobacter jejuni–an emerging foodborne pathogen. Emerg Infect Dis 5(1):28–35
5. Mintmier B, McGarry JM, Bain DJ, Basu P (2021) Kinetic consequences of the endogenous ligand to molybdenum in the DMSO reductase family: a case study with periplasmic nitrate reductase. J Biol Inorg Chem 26(1):13–28
6. Coelho C, Romao MJ (2015) Structural and mechanistic insights on nitrate reductases. Protein Sci 24(12):1901–1911
7. Gonzalez PJ, Rivas MG, Mota CS, Brondino CD, Moura I, Moura JJG (2013) Periplasmic nitrate reductases and formate dehydrogenases: biological control of the chemical properties of Mo and W for fine tuning of reactivity, substrate specificity and metabolic role. Coord Chem Rev 257(2):315–331
8. Najmudin S, Gonzalez PJ, Trincao J, Coelho C, Mukhopadhyay A, Cerqueira NM, Romao CC, Moura I, Moura JJ, Brondino CD, Romao MJ (2008) Periplasmic nitrate reductase revisited: a sulfur atom completes the sixth coordination of the catalytic molybdenum. J Biol Inorg Chem 13(5):737–753
9. Yang J, Mintmier B, Kc K, Metzger MC, Radhakrishnan M, McGarry J, Wilcoxen J, Basu P, Kirk ML (2024) Active site characterization of a campylobacter jejuni nitrate reductase variant provides insight into the enzyme mechanism. Inorg Chem 63:13191
10. Giri NC, Mintmier B, Radhakrishnan M, Mielke JW, Wilcoxen J, Basu P (2024) The critical role of a conserved lysine residue in periplasmic nitrate reductase catalyzed reactions. J Biol Inorg Chem 23:1
11. Mintmier B, McGarry JM, Sparacino-Watkins CE, Sallmen J, Fischer-Schrader K, Magalon A, McCormick JR, Stolz JF, Schwarz G, Bain DJ, Basu P (2018) Molecular cloning, expression and biochemical characterization of periplasmic nitrate reductase from Campylobacter jejuni. FEMS Microbiol Lett 365(16):fny151
12. Brige A, Leys D, Meyer TE, Cusanovich MA, Van Beeumen JJ (2002) The 1.25 A resolution structure of the diheme NapB subunit of soluble nitrate reductase reveals a novel cytochrome c fold with a stacked heme arrangement. Biochemistry 41(15):4827–4836
13. Kirk ML, Hille R (2022) Spectroscopic studies of mononuclear molybdenum enzyme centers. Molecules. https://doi.org/10.3390/molecules27154802
14. Ingersol LJ, Yang J, Kc K, Pokhrel A, Astashkin AV, Weiner JH, Johnston CA, Kirk ML (2020) Addressing ligand-based redox in molybdenum-dependent methionine sulfoxide reductase. J Am Chem Soc 142(6):2721–2725
15. Shanmugam M, Wilcoxen J, Habel-Rodriguez D, Cutsail III GE, Kirk ML, Hoffman BM, Hille R (2013) C-13 and Cu-63, Cu-65 ENDOR studies of CO Dehydrogenase from Oligotropha carboxidovorans Experimental Evidence in Support of a Copper-Carbonyl Intermediate. J Am Chem Soc 135(47):17775–17782
16. George GN, Hilton J, Temple C, Prince RC, Rajagopalan KV (1999) Structure of the molybdenum site of dimethyl sulfoxide reductase. J Am Chem Soc 121(6):1256–1266
17. Michaelis L, Hill ES (1933) The viologen indicators. J Gen Physiol 16(6):859–873
18. Aasa R, Vänngård, t. (1975) EPR signal intensity and powder shapes: A reexamination. J Mag Res. https://doi.org/10.1016/0022-2364(75)90045-1
19. Arnoux P, Sabaty M, Alric J, Frangioni B, Guigliarelli B, Adriano JM, Pignol D (2003) Structural and redox plasticity in the heterodimeric periplasmic nitrate reductase. Nat Struct Biol 10(11):928–934
20. Jormakka M, Tornroth S, Byrne B, Iwata S (2002) Molecular basis of proton motive force generation: Structure of formate dehydrogenase-N. Science 295(5561):1863–1868
21. Gonzalez PJ, Rivas MG, Brondino CD, Bursakov SA, Moura I, Moura JJ (2006) EPR and redox properties of periplasmic nitrate reductase from Desulfovibrio desulfuricans ATCC 27774. J Biol Inorg Chem 11(5):609–616
22. Fourmond V, Burlat B, Dementin S, Arnoux P, Sabaty M, Boiry S, Guigliarelli B, Bertrand P, Pignol D, Leger C (2008) Major Mo(V) EPR signature of Rhodobacter sphaeroides periplasmic nitrate reductase arising from a dead-end species that activates upon reduction Relation to other molybdoenzymes from the DMSO reductase family. J Phys Chem B 112(48):15478–15486
23. Butler CS, Charnock JM, Bennett B, Sears HJ, Reilly AJ, Ferguson SJ, Garner CD, Lowe DJ, Thomson AJ, Berks BC, Richardson DJ (1999) Models for molybdenum coordination during the catalytic cycle of periplasmic nitrate reductase from Paracoccus denitrificans derived from EPR and EXAFS spectroscopy. Biochemistry 38(28):9000–9012
24. Bennett B, Berks BC, Ferguson SJ, Thomson AJ, Richardson DJ (1994) Mo(V) electron paramagnetic resonance signals from the periplasmic nitrate reductase of Thiosphaera pantotropha. Eur J Biochem 226(3):789–798
25. Bradford MM (1976) A rapid and sensitive method for the quantitation of microgram quantities of protein utilizing the principle of protein-dye binding. Anal Biochem 72(1–2):248–254
26. Stoll S (2011) High-field EPR of bioorganic radicals. In: Gilbert BC, Murphy V (eds) Electron Paramagnetic Resonnace. Royal Society of Chemistry, Cambridge
27. Biaso F, Burlat B, Guigliarelli B (2012) DFT investigation of the molybdenum cofactor in periplasmic nitrate reductases: structure of the Mo(V) EPR-active species. Inorg Chem 51(6):3409–3419
28. Garton SD, Hilton J, Oku H, Crouse BR, Rajagopalan KV, Johnson MK (1997) Active site structures and catalytic mechanism of Rhodobacter sphaeroides dimethyl sulfoxide reductase as revealed by resonance Raman spectroscopy. J Am Chem Soc 119(52):12906–12916
29. McAlpine AS, McEwan AG, Shaw AL, Bailey S (1997) Molybdenum active centre of DMSO reductase from Rhodobacter capsulatus: crystal structure of the oxidised enzyme at 1.82-Å resolution

and the dithionite-reduced enzyme at 2.8-Å resolution. JBIC J Biol Inorg Chem. https://doi.org/10.1007/s007750050185
30. Schindelin H, Kisker C, Hilton J, Rajagopalan KV, Rees DC (1996) Crystal structure of DMSO reductase: redox-linked changes in molybdopterin coordination. Science 272(5268):1615–1621
31. Sung KM, Holm RH (2001) Oxo transfer reactions mediated by bis(dithiolene)tungsten analogues of the active sites of molybdoenzymes in the DMSO reductase family: comparative reactivity of tungsten and molybdenum. J Am Chem Soc 123(9):1931–1943
32. Tenderholt AL, Wang J-J, Szilagyi RK, Holm RH, Hodgson KO, Hedman B, Solomon EI (2010) Sulfur K-Edge X-ray absorption spectroscopy and density functional calculations on Mo(IV) and Mo(VI)=O Bis-dithiolenes: insights into the mechanism of Oxo transfer in DMSO reductase and related functional analogues. J Am Chem Soc 132(24):8359–8371
33. Cobb N, Conrads T, Hille R (2005) Mechanistic studies of Rhodobacter sphaeroides Me2SO reductase. J Biol Chem 280(12):11007–11017
34. Benson N, Farrar JA, McEwan AG, Thomson AJ (1992) Detection of the optical bands of molybdenum(V) in DMSO reductase (Rhodobacter capsulatus) by low-temperature MCD spectroscopy. FEBS Lett 307(2):169–172
35. Kilpatrick L, Rajagopalan KV, Hilton J, Bastian NR, Stiefel EI, Pilato RS, Spiro TG (1995) Resonance raman spectroscopic characterization of the molybdopterin active site of DMSO reductase. Biochemistry 34(9):3032–3039
36. Schultz BE, Hille R, Holm RH (2002) Direct oxygen atom transfer in the mechanism of action of rhodobacter sphaeroides dimethyl sulfoxide reductase. J Am Chem Soc 117(2):827–828
37. Ryde U, Schulzke C, Starke K (2009) Which functional groups of the molybdopterin ligand should be considered when modeling the active sites of the molybdenum and tungsten cofactors? a density functional theory study. J Biol Inorg Chem 14(7):1053–1064
38. Hadt RG, Nemykin VN, Olsen JG, Basu P (2009) Comparative calculation of EPR spectral parameters in [Mo(V)OX4]-, [Mo(V)OX5]2-, and [Mo(V)OX4(H2O)]- complexes. Phys Chem Chem Phys 11(44):10377–10384
39. Nemykin VN, Sabin JR, Kail BW, Upadhyay A, Hendrich MP, Basu P (2023) Influence of the ligand-field on EPR parameters of cis- and trans-isomers in Mo(V) systems relevant to molybdenum enzymes: Experimental and density functional theory study. J Inorg Biochem 245:112228
40. Srivastava AP, Allen JP, Vaccaro BJ, Hirasawa M, Alkul S, Johnson MK, Knaff DB (2015) Identification of amino acids at the catalytic site of a ferredoxin-dependent cyanobacterial nitrate reductase. Biochemistry 54(36):5557–5568
41. Lamy MT, Gutteridge S, Bray RC (1980) Electron-paramagnetic-resonance parameters Of molybdenum(V) in sulfite oxidase from chicken liver. Biochemical Journal 185(2):397–403
42. Reschke S, Niks D, Wilson H, Sigfridsson KG, Haumann M, Rajagopalan KV, Hille R, Leimkuhler S (2013) Effect of exchange of the cysteine molybdenum ligand with selenocysteine on the structure and function of the active site in human sulfite oxidase. Biochemistry 52(46):8295–8303
43. Yang J, Rothery R, Sempombe J, Weiner JH, Kirk ML (2009) Spectroscopic characterization of YedY: the role of sulfur coordination in a Mo(V) sulfite oxidase family enzyme form. J Am Chem Soc 131(43):15612
44. Cerqueira NM, Gonzalez PJ, Brondino CD, Romao MJ, Romao CC, Moura I, Moura JJ (2009) The effect of the sixth sulfur ligand in the catalytic mechanism of periplasmic nitrate reductase. J Comput Chem 30(15):2466–2484
45. Maillard J, Spronk CA, Buchanan G, Lyall V, Richardson DJ, Palmer T, Vuister GW, Sargent F (2007) Structural diversity in twin-arginine signal peptide-binding proteins. Proc Natl Acad Sci U S A 104(40):15641–15646
46. Jepson BJ, Mohan S, Clarke TA, Gates AJ, Cole JA, Butler CS, Butt JN, Hemmings AM, Richardson DJ (2007) Spectropotentiometric and structural analysis of the periplasmic nitrate reductase from escherichia coli. J Biol Chem 282(9):6425–6437
47. Hille R, Niks D (2022) Application of EPR and related methods to molybdenum-containing enzymes. Methods Enzymol 666:373–412
48. Harmer JR, Hakopian S, Niks D, Hille R, Bernhardt PV (2023) Redox characterization of the complex molybdenum enzyme formate dehydrogenase from cupriavidus necator. J Am Chem Soc 145(47):25850–25863
49. Maia LB, Moura JJ, Moura I (2015) Molybdenum and tungsten-dependent formate dehydrogenases. J Biol Inorg Chem 20(2):287–309

**Publisher's Note** Springer Nature remains neutral with regard to jurisdictional claims in published maps and institutional affiliations.

Springer Nature or its licensor (e.g. a society or other partner) holds exclusive rights to this article under a publishing agreement with the author(s) or other rightsholder(s); author self-archiving of the accepted manuscript version of this article is solely governed by the terms of such publishing agreement and applicable law.